CHEMISTRY OF MATERIALS

ARTICLE

pubs.acs.org/cm

Nitrogen-Doped Single-Walled Carbon Nanotube Thin Films Exhibiting Anomalous Sheet Resistances

Toma Susi,[*,†] Antti Kaskela,[†] Zhen Zhu,[†] Paola Ayala,[‡] Raul Arenal,[§,∥] Ying Tian,[†] Patrik Laiho,[†] Juha Mali,[†] Albert G. Nasibulin,[†] Hua Jiang,[†] Giorgio Lanzani,[⊥,#] Odile Stephan,[▽] Kari Laasonen,[#,○] Thomas Pichler,[‡] Annick Loiseau,[§] and Esko I. Kauppinen[*,†]

[†]NanoMaterials Group, Department of Applied Physics, Aalto University School of Science, P.O. Box 15100, FI-00076 Aalto, Espoo, Finland

[‡]University of Vienna, Faculty of Physics, Strudlhofgasse 4, 1090 Wien, Austria

[§]LEM, UMR 104 ONERA-CNRS, 29 Avenue de la Division Leclerc, 92322 Châtillon, France

[∥]LMA, Instituto de Nanociencia de Aragon, U. Zaragoza, c/Mariano Esquillor, 50018 Zaragoza, Spain

[⊥]Thule Institute, University of Oulu, P.O. Box 7300, FI-90014, University of Oulu, Finland

[#]Department of Chemistry, University of Oulu, P.O. Box 3000, FI-90014, University of Oulu, Finland

[▽]LPS, UMR 8502 CNRS, Université Paris Sud XI, Bâtiment 510, 91405 Orsay, France

[○]Department of Chemistry, Aalto University School of Chemical Technology, P.O. Box 16100, FI-00076 Aalto, Espoo, Finland

Supporting Information

ABSTRACT: Nitrogen-doped single-walled carbon nanotubes (N-SWCNTs) were synthesized using a floating catalyst aerosol chemical vapor deposition method, with carbon monoxide as the carbon source, ammonia as the nitrogen source, and iron particles derived from evaporated iron as the catalyst. The material was deposited on various substrates as grown directly from the gas phase as films and subsequently characterized by Raman and optical absorption spectroscopies, sheet resistance measurements, electron microscopy, energy-loss spectroscopy, and X-ray photoelectron spectroscopy.

The sheet resistance measurements revealed that the doped films had unexpectedly high resistances. This stands in contrast to the case of N-MWCNT films, where decreased resistance has been reported with N-doping. To understand this effect, we developed a resistor network model, which allowed us to disentangle the contribution of bundle−bundle contacts when combined with data on undoped films. Assuming doping does not significantly change the contacts, the increased resistances of the doped films are likely due to enhanced carrier scattering by defect sites in the nanotubes. This work represents the first experimental report on macroscopic N-SWCNT thin films.

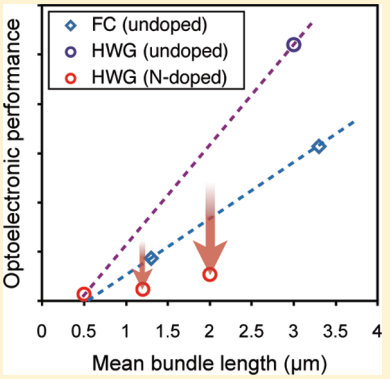

KEYWORDS: nitrogen doping, gas-phase aerosol CVD, SWCNT, thin films

1. INTRODUCTION

Harnessing the full potential of carbon nanotubes (CNTs) hinges on finding the means to control the electronic properties of an ensemble of synthesized nanotubes. Much effort has been directed to controlling the chirality of produced nanotubes during synthesis, to some extent successfully.[1−4] Another possible way to control the electronic properties of nanotubes is by substitutional doping with foreign chemical elements. The two practical candidates are the nearest neighbors to carbon in the periodic table, boron and nitrogen. Nitrogen in particular has attracted much attention[5−10] because of its suitable atomic size and envisaged applications for N-doped nanotubes.[11,12] Substitutional doping is distinct from other methods of donating charge to the nanotubes, such as charge transfer by redox-active molecules (chemical doping), simple gating, or electrochemical charging.

A variety of methods[13] are available for the synthesis of nitrogen-doped multiwalled carbon nanotubes (N-MWCNTs). However, synthesis of nitrogen-doped single-walled nanotubes (N-SWCNTs) is much more difficult,[14−16] particularly using chemical vapor deposition[17−20] (CVD).

Apart from their individual electrical character, the positions, lengths, bundling, and orientations of nanotubes show considerable variability, which makes reliable and cheap fabrication of devices with reproducible electrical behavior difficult. Therefore random carbon nanotube networks (CNTNs) have attracted considerable interest as the first viable technological avenue for CNT applications. In this context, many promising applications have been demonstrated such

Received: January 13, 2011
Revised: February 25, 2011
Published: March 21, 2011

as optically transparent conductors,[21,22] transparent transistors,[23,24] organic light emitting diodes,[25] and chemical sensors.[26]

It has been expected that doping might enhance the optoelectronic properties of nanotube films, specifically for use as transparent conducting electrodes (TCEs). There are some reports on N-MWCNT films where slight enhancement has been observed.[27] The case of N-SWCNTs is much less known.

Here, we present a new approach to directly synthesize thin films of N-SWCNTs using a gas-phase floating catalyst CVD method, where carbon monoxide (CO) acts as the carbon source, ammonia (NH_3) as the nitrogen source, and iron particles derived from physical nucleation of evaporated iron as the catalyst (dubbed the "hot wire generator" (HWG) method[28]). The material is dry-deposited directly from the reactor as films on various substrates, and no solution processing, sonication, or centrifugation is applied. This ensures that the intrinsic properties of the material are preserved, which we have studied using Raman and optical absorption spectroscopies, sheet resistance measurements, electron microscopy, energy-loss spectroscopy, and X-ray photoelectron spectroscopy.

Most importantly, we analyze the optoelectronic properties of these films in detail, showing that nitrogen doping seems to cause a loss of performance compared to undoped films. The analysis shows that this effect is likely due to an increase in the resistances of the bundles and not to the geometric factors related to bundle lengths and number of contacts. This suggests that the intrabundle resistances are higher for N-SWCNTs than those for pristine SWCNTs, which may be due to enhanced carrier scattering by defect sites in the nanotubes.

2. EXPERIMENTAL METHODS

2.1. Synthesis. The synthesis method has been adapted from ref 28. Briefly, catalyst particles are grown in situ by nucleation from iron vapor evaporated from a resistively heated iron wire (the HWG) of 0.25 mm diameter (Goodfellow, 99.5% purity), inserted into an ambient pressure laminar flow reactor in a ceramic inner tube. The wire is protected by a 400 cm^3/min H_2/Ar flow (7/93%). An additional outer gas flow of 400 cm^3/min CO provides the carbon source. The reactor maximum wall temperature was set to 890 °C, which has been found[22] to be the optimal temperature to obtain long and high quality pristine nanotubes using this setup with 1500 ppm of added CO_2. Previously, it was also noticed that even very small amounts of introduced NH_3 have a severe effect on nanotube production in a floating catalyst environment,[29] with the exact maximum usable amount depending on the gas mix and the catalyst particle production method. To accurately introduce very small amounts of ammonia, a dilution system was thus used. Set flow rates (0 to 2.0 cm^3/min) of ammonia were diluted with 80 cm^3/min of Ar. Before introducing the mixed flow into the reactor, 65 cm^3/min was diverted into vacuum. The resulting inlet flow rates of ammonia were validated by Fourier transform infrared spectroscopy, and good control was achieved in the 0−500 ppm range. The role of NH_3 is dual, as it acts as the nitrogen doping source[30,31] as well as an etching agent,[29] while CO_2 acts only as an etching agent.[32,33] The outlet flow was mixed with a 3000 cm^3/min N_2 flow using a porous tube dilutor. Samples were collected directly at the reactor outlet either by an electrostatic precipitator[24] (ESP) onto carbon-coated copper transmission electron microscopy (TEM) grids or onto SiO_2 or by filtering onto microporous membrane filter papers (Millipore). Optically opaque films could be collected on 13 mm diameter filters in about 1 h using a 1500 cm^3/min collector flow. Typical collection times were 30 min, and the characterization results shown below constitute a representative set of samples.

2.2. Characterization. Raman spectra for samples collected on the membrane filters were measured at ambient conditions using a 632.81 nm HeNe laser (Jobin Yvon Labram 300, Stigmatic 300 spectrograph). Optical absorption spectra were measured using a double line UV−vis−NIR spectrophotometer (Perkin-Elmer lambda 900) after transferring the films from the filters onto quartz glass plates by modest pressure (~10^3 Pa). The sheet resistances of the films were determined by 4-probe measurement (Agilent 34410A multimeter and Jandel Engineering, Ltd. four-point probe). To study the bundle length distributions, sparse submonolayer films were concurrently deposited by ESP (30 s collection time, 300 cm^3/min sample flow, 6 kV voltage) onto SiO_2 and observed by scanning electron microscopy (SEM, Jeol JSM-7500F). Additional TEM observations were conducted on the TEM grid samples collected by ESP (5 min collection time, 300 cm^3/min sample flow, 1.5 kV voltage) using a Jeol JEM-2200FS double aberration-corrected TEM, which was operated at 80 kV and carefully calibrated with Au reference particles.

Electron energy-loss spectra were recorded using a VG-HB501 dedicated scanning transmission electron microscope (STEM) equipped with a cold field emission gun (FEG), operated at 100 keV with an energy resolution close to 0.7−0.8 eV in the core-loss region. The convergence angle on the sample and collection angle of the spectrometer were 15 and 24 mrad, respectively. The spectroscopic information was obtained using the spectrum-imaging (SPIM) acquisition mode.[34,35] For the spectra acquisition, a slightly defocused electron probe was scanned in a small area of a few nm^2.

To determine the overall nitrogen content within the samples, we employed X-ray photoelectron spectroscopy (XPS) using a PHI 5600 spectrometer equipped with a monochromatic Al Kα source (1486.6 eV) operating with a base pressure of 10^{-9} mbar and an overall spectral resolution of 0.5 eV.

3. THEORETICAL METHODS

The optical and electrical characteristics of SWCNT films thicker than a few separate monolayers can be described by bulk material conductivity laws.[22] The quality of transparent conducting thin films is usually stated as their sheet resistance (R_s) versus optical transmittance (T%) at a reference wavelength (550 nm). By starting from the Beer−Lambert law for the absorbance $A(\lambda)$ a film of thickness L

$$A(\lambda) = -\ln T(\lambda) = \varepsilon(\lambda)\mathrm{d}L \quad (1)$$

for the wavelength λ, and the definition of sheet resistance R_s (or sheet conductance, σ_s)

$$R_s = 1/\sigma_s = \rho_e a/aL = \rho_e/L = 1/\sigma L \quad (2)$$

where a is the sheet area, σ is the electrical dc conductance, and ρ_e the electrical resistivity, we can relate the two measures to each other by

$$R_s = -\varepsilon\rho/(\sigma \ln T) = -1/(K \ln T) \quad (3)$$

where ε is the Beer−Lambert extinction coefficient and ρ is the film density, which is not generally known. Nevertheless, we can use the ratio

$$K = \sigma/\varepsilon\rho \quad (4)$$

calculated from eq 3 using experimentally measurable resistance and transmittance values as a figure of merit for the optoelectronic performance of the films. This relation clearly shows that for structurally similar films with similar values of ε and ρ, the R_s/T ratio is controlled by the conductance σ, which further depends on factors such as the morphology of the random network comprising a SWCNT film.[36]

We studied the dependence of σ on the network morphology using a random resistor network model. The key assumption in our model, motivated by measurements of the resistance of SWCNT bundles[37] and bundle−bundle contact resistances,[38] is

that the electrical resistance along SWCNT bundles is low compared to that of the junctions, and that the bundle network can thus be described by an analogous network of resistors representing the contact resistances, ideally connected by the bundles.

We represent the network as an equivalent circuit in which the nodes represent CNT bundles and resistors between them represent bundle−bundle contacts. The circuit is created by randomly and isotropically generating line segments with an experimentally motivated log-normal length distribution in a square area, registering intersections between the segments and mapping each segment as a node and each intersection as a resistor. Finally, intersections with the upper and lower edges of the square are registered. The resistance is calculated by elementary circuit analysis via the conductance matrix G, using one horizontal edge of the square as the ground and calculating the node voltage at the opposing edge by solving the linear system $Gv = i$, where v is the node voltage vector and i is a source vector, and where $i(1) = 1$ and 0 otherwise.

We studied the dependence of the conductance and the network connectivity, defined as the average number of intersections per bundle, on the average bundle length by generating networks with varying line segment length distributions, averaging over 100 individual simulations per distribution. In all simulations, a fixed density of (total segment length)/(square area) was used and set high enough to make the networks nearly or completely connected and thus far above the percolation threshold (where only few conducting pathways exist through the network). To ensure the nonsingularity of G, stray segments not connected by any path to the ground and reference nodes were eliminated. Additionally, the dependence of the network connectivity on average bundle diameter was studied by generating networks where the bundles are represented by tilted rectangles instead of simple line segments. Because we have concentrated in obtaining the general forms of scaling between the mentioned parameters, the contact resistances in the simulations were normalized to 1 Ω in all cases. It is worth noting that contact resistances have been experimentally shown to change dramatically with large changes in the diameters of the connected bundles.[38] In our simulation, the bundle diameters were thought to be fixed and small compared to the lengths and the orientations perfectly isotropical; therefore, these variations average out.

4. RESULTS

4.1. Characterization. Representative scanning and transmission electron microscopy images of the 0 and 200 ppm NH_3 sample are shown in Figure 1. The SEM images were recorded directly on the samples deposited on membrane filters. The optical, spectroscopic, and sheet resistance measurements in the text below were performed on the membrane filter samples. It should be again noted that the material has not been treated or purified in any way, and even so, the optoelectronic properties of the undoped films are excellent[22] (see also Section 4.2). The tubes were typically found in small bundles, with diameters determined by TEM to be 6.1 ± 3.0 nm for the 0 ppm NH_3 sample and slightly smaller, 3.7 ± 1.7 nm, for the 200 ppm NH_3 sample (50 bundle statistics each). Individual nanotubes could also be found quite easily (see also Figures S1 and S2 of the Supporting Information). There seems to be slightly more visible impurities on the undoped bundles, while the doped samples exhibited somewhat larger inactive catalyst particles, as well as shorter bundles. The other doped samples appear similar to the 200 ppm NH_3 one.

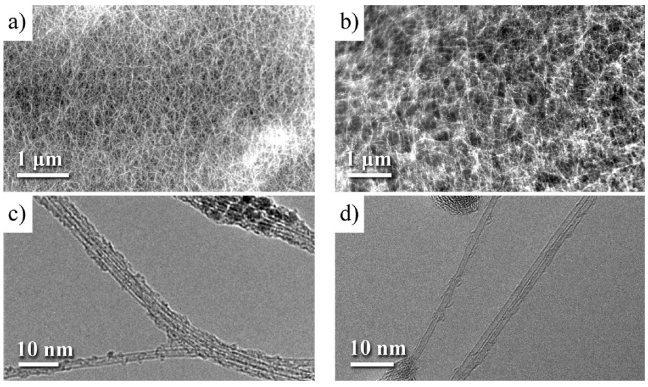

Figure 1. Scanning (a,b) and transmission (c,d) electron microscope images of nanotube bundles in samples synthesized with (a) and (c) no NH_3 and (b) and (d) 200 ppm NH_3.

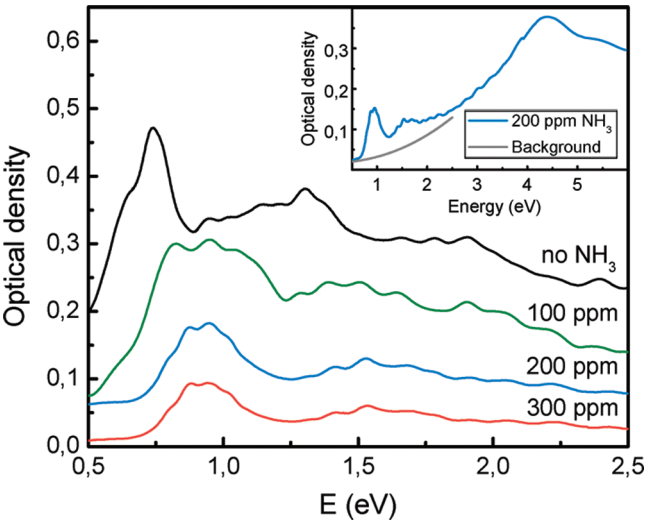

Figure 2. Optical absorption spectra of samples synthesized with 0, 100, 200, and 300 ppm NH_3. The backgrounds have been subtracted (following ref 40) and the spectra offset for clarity. The inset shows the raw spectrum for the 200 ppm NH_3 sample in the range of 0.5 to 6 eV, along with the background that was subtracted in the main figure.

Collecting statistically sufficient data in TEM is very time-consuming. Therefore optical absorption spectra (OAS, Figure 2) were used to evaluate the diameter distributions of the SWCNT films because all types of nanotubes have transitions in the UV−vis−NIR region.[39] As shown in Figure 2, the absorption peaks shift to higher energy when the N precursor is introduced, implying a decrease in the diameter of the SWCNTs. The OAS of samples synthesized with 200 and 300 ppm NH_3 present quite similar profiles, showing narrower peak widths than the one collected with 100 ppm NH_3. Recently, a new method for quantifying the diameter distributions of SWNTs has been developed on the basis of optical absorption spectra.[40] Following this method, we evaluated the mean diameters of the nanotubes in the 0, 100, 200, and 300 ppm NH_3 samples to be 1.4 ± 0.3, 1.2 ± 0.3, 1.1 ± 0.2, and 1.1 ± 0.2 nm, respectively. Similar findings of a decrease in diameter with an increasing N precursor amount have before been reported.[19,20,41] Practically no tubes were produced with more than 300 ppm NH_3.

Because the OAS method has been extensively validated only for undoped tubes,[40] we further verified the diameter distribution

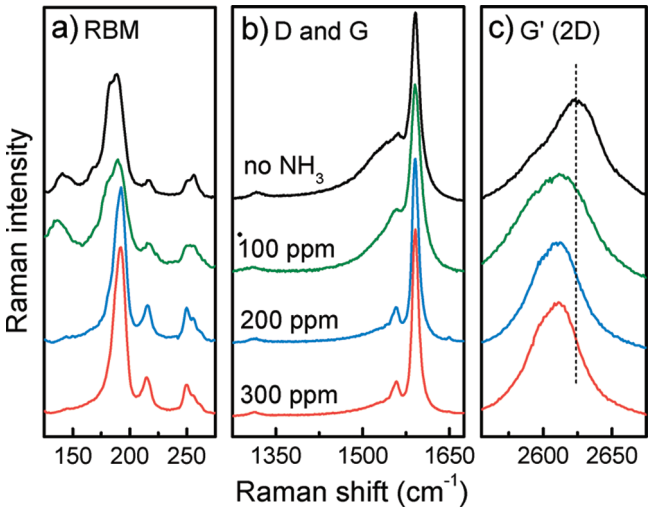

Figure 3. Raman spectra recorded with a 632.81 nm excitation from samples synthesized with 0, 100, 200, and 300 ppm NH_3. The panels (a)−(c) show the RBM, D and G, and G′ (2D) regions of the Raman response.

of the 200 ppm NH_3 sample by independently measuring the diameters of 56 individual SWCNTs in the sample by HR-TEM. A representative example can be found in Figure S1 of the Supporting Information. The corresponding micrographs for the undoped 0 ppm NH_3 sample are shown in Figure S2 of the Supporting Information. The diameter distributions of the 200 ppm NH_3 sample thus obtained by OAS and TEM are shown in Figure S3 of the Supporting Information. Not only are the mean diameters and variances equal, even the shape of the distribution matches remarkably well.

Raman spectra were recorded for samples synthesized with 0, 100, 200, and 300 ppm NH_3 using a 632.81 nm (1.96 eV) excitation. Figure 3 contains the features characteristic of SWCNTs.[42] The left panel (Figure 3a) shows the radial breathing modes (RBM). The peak positions and intensities in the RBM region provide an idea of the diameters corresponding to nanotubes in resonance with the specific excitation used. The lowering of the left side peak supports the conclusion of decreasing nanotube diameter with increasing NH_3 already demonstrated by OAS and TEM analyses. The middle panel (Figure 3b) shows the disorder-induced Raman peak (D) and the G band, features which are observed in various carbon systems, but which are specifically related to SWCNTs here.

The G′ (2D) band is shown in panel (c) of Figure 3. Changes of the G′ band have been suggested as a signature of doping in SWCNTs.[43] Although further studies are required on this topic, we note that there is a downshift of the main peak of the G′ band of $\Delta\omega_{G'} \approx -15\ \mathrm{cm}^{-1}$ compared to that of the undoped material in the samples synthesized with NH_3. However, some shift would also be expected with the changing nanotube diameter. To roughly estimate this effect for the single excitation used, we used the relation[44]

$$\omega_{G'} = C_1 - C_2/d \qquad (5)$$

with[45] $C_1 = 2642.8\ \mathrm{cm}^{-1}$ (determined for the 1.96 eV excitation used) and $C_2 = 35.4\ \mathrm{cm}^{-1}$ nm. Inspection of the almost identical RBM features of the 0 and 100 ppm NH_3 samples (Figure 3a), with a G′ shift of almost $-15\ \mathrm{cm}^{-1}$, would suggest that changes in the Raman resonant nanotubes' diameters do not explain the changes in the G′ band.

However, because the resonance window of G′ is broader than that of the RBM, it is more relevant to look at changes in the entire diameter distribution. Using the mean diameters determined from the OAS in eq 5, still a shift of only about $-6\ \mathrm{cm}^{-1}$ would be expected with a decrease in diameter from 1.4 to 1.1 nm. This is clearly not enough to explain the observed shift. Additional spectroscopic studies are required to make conclusions about the possibility of using the G′ signal as a metrological tool for inspecting bulk samples of doped nanotubes.

As stated above, practically no nanotubes were produced with more than 300 ppm NH_3. However, the Raman spectra (Figure 3) showed little change with increasing NH_3 amount up to 300 ppm. To understand the sudden disruption of production with higher concentrations, we deposited sparse submonolayer networks synthesized with each concentration of NH_3 onto SiO_2 and studied the bundle length distributions by measuring bundle lengths by SEM (50 bundle statistics each). We found that with increasing NH_3, the bundles became progressively shorter (Table 1), decreasing from 3.0 μm in the 0 ppm NH_3 sample to 0.5 μm in the 300 ppm NH_3 sample.

The measured sheet resistances as well as the transmittances (at 550 nm) determined from the OAS spectra are shown in Table 1, along with the figures of merit K calculated from eq 3. Note that the films collected with 200 and 300 ppm NH_3 are significantly thinner, indicative of a decreased yield. The analysis of the optoelectronic properties of the films is discussed in Section 4.2.

Turning now to the study of N incorporation in the SWCNTs, panel (a) of Figure 4 displays an EEL spectrum (C− and N−K edges), which is a sum of 4 EEL spectra with an acquisition time of 2 s each, recorded on the marked area shown in the high angle annular dark field micrograph (Figure 4b) of a bundle of N-SWCNTs synthesized with 200 ppm NH_3. The energy loss near-edge feature of the C−K edge consisted of a π^* peak at ∼285 eV and a well-defined σ^* band starting at ∼292 eV. These signatures are typical for the sp^2 hybridization of the C atoms in a graphitic network. From the N−K edges (Figure 4a inset for the 200 ppm NH_3 sample), we calculated[13,14,34] that the total nitrogen concentration in different bundles of the 100 ppm NH_3 sample ranged from 0.3 to 2.0 at. %, with an average of about 1.2 at. %. A similar analysis for the 200 ppm NH_3 sample gave an estimate of 1.7 at. %. The 300 ppm NH_3 sample was not stable enough under the electron beam to measure EELS.

As an additional analytic technique, XPS was used to estimate the overall N concentration in our films. For this purpose, we have specifically taken into account the differing atomic cross sections of C and N. We carefully considered the carbon core signal, where it is well established that different carbon molecular structures have defined and characteristic C1s line shapes, giving essential information regarding the kind of SWCNT material studied.[46] For this reason, the C1s is used as a prerequisite for any further measurement of nitrogen heteroatoms. The spectral deconvolution for the nitrogen core level signal (N1s) contains approximately equal contributions of 398.6 and 400.5 eV binding energies, as has been described previously.[15,47] The total nitrogen concentration in the films was determined to be 0.2 at. % in the 100 ppm NH_3 sample, 0.7 at. % in the 200 ppm NH_3 sample, and 1.1 at. % in the 300 ppm NH_3 sample. It is important to remark here again that the sample produced with 300 ppm NH_3 showed more instability when exposed to the electron beam in

Table 1. Properties of CNT films synthesized with 0, 100, 200, and 300 ppm NH_3 and collected for 30 min each[a]

	average N content (at. %)						
NH_3 (ppm)	EELS	XPS	mean diameter ± variance (nm)	T @ 550 nm (%)	bundle length ± std. dev. (μm)	4-point R (kΩ/□)	K (□/kΩ)
0	–	–	1.4 ± 0.3	43	3.0 ± 1.1	0.2	5.20
100	1.2	0.2	1.2 ± 0.3	45	2.1 ± 0.9	2.3	0.54
200	1.7	0.7	1.1 ± 0.2	72	1.2 ± 0.7	12.3	0.24
300	–	1.1	1.1 ± 0.2	78	0.5 ± 0.4	29.6	0.12

[a] The columns show ammonia concentration, average nitrogen content determined by EELS and XPS, mean nanotube diameters determined40 from OAS (Figure 2), transmittance of 550 nm light, mean bundle lengths determined by SEM, sheet resistances of the films measured by 4-probe measurement, and optoelectronic figures of merit K for the films calculated from eq 3.

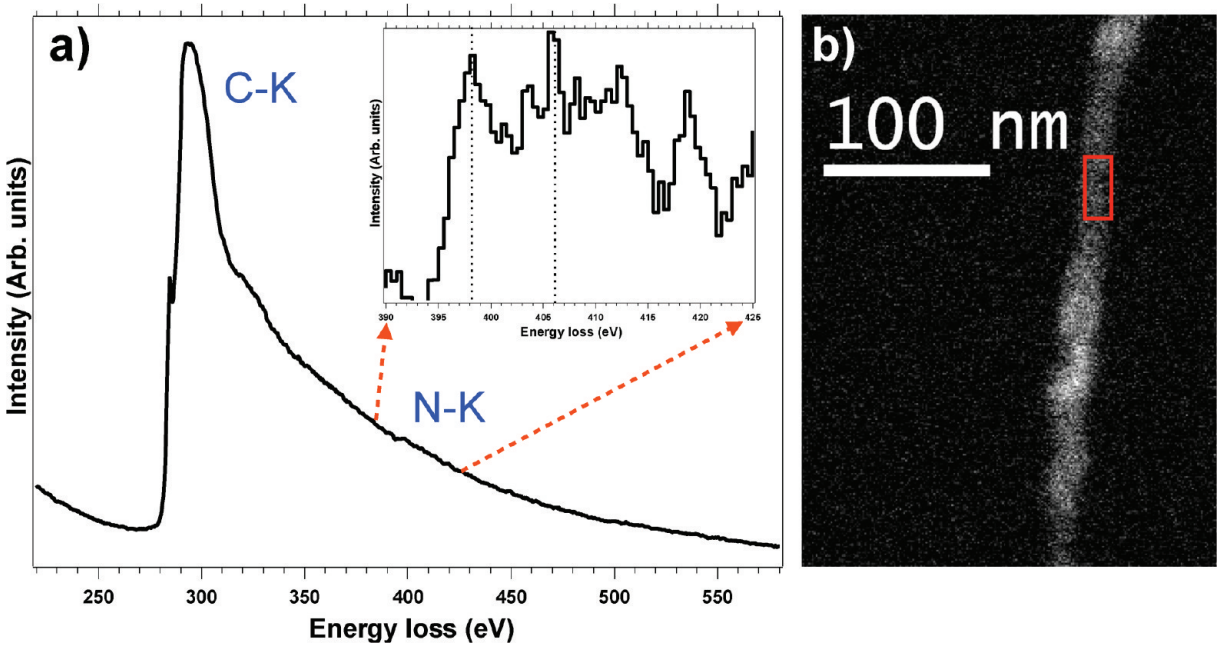

Figure 4. (a) Sum of 4 EEL spectra (C− and N−K edges) with an acquisition time of 2 s each, recorded on the marked area shown in the (b) high angle annular dark field micrograph of a bundle of N-SWCNTs synthesized at with 200 ppm NH_3. The inset of (a) shows a magnification of the N−K edge after background subtraction.

TEM-EELS. Only in this case a slight upshift was detected in the C1 line, which suggests the formation of defective sites on the nanotubes, as reported in other studies related to N-SWCNTs.[15,47] This would explain the observed instability of that sample under the electron beam.

4.2. Sheet Resistance Analysis. Figure 5 shows an example of a line segment network generated by our resistor network code (Section 3). Figure S4 of the Supporting Information shows the dependence of network conductance σ on average line segment length $\langle l \rangle$, exhibiting a linear dependence over the experimentally relevant range of 1−4 μm; simulations with <l> of 0.5 μm did not converge. In all cases, random log-normal length distributions

$$f(x;\mu,s) = \frac{1}{xs\sqrt{2\pi}}\, e^{-(\ln x - \mu)^2/2s^2}, \quad x > 0 \qquad (6)$$

were used, where μ and s are the mean and standard deviation of the natural logarithm of the dimensionless length x, respectively. The values for the standard deviations were calculated from the experimental bundle length distributions (Table 1). The nonzero intercept of the x-axis is to be expected on the basis of percolation arguments. The network connectivity, defined as the average amount of contacts per line segment, was likewise found to depend on $\langle l \rangle$ linearly, suggesting that network conductance is directly determined on the connectivity.

We also ran simulations with rectangles of finite widths at fixed length. Even a decrease of aspect ratio from 1000 to 100 resulted in an increase of connectivity of only 3.5%. This implies that changes in network connectivity due to changes in the diameter distribution are negligible compared to changes caused by a varying length distribution. Thus, the decrease of bundle diameter in the doped nanotube samples from 6.1 (0 ppm NH_3) to 3.7 nm (200 ppm NH_3) should not cause discernible changes in the connectivity (and thus figure of merit) on the basis of the aspect ratio simulations.

To compare the simulations with experimental data, the sheet resistance and transmittance values for undoped (that is, normal) SWCNT films were compared to those reported above for the doped SWCNT films synthesized with 100−300 ppm NH_3 (Table 1). As the undoped reference films, two sets of samples were used. The first were films of varying thickness synthesized previously with a very similar floating catalyst CVD system

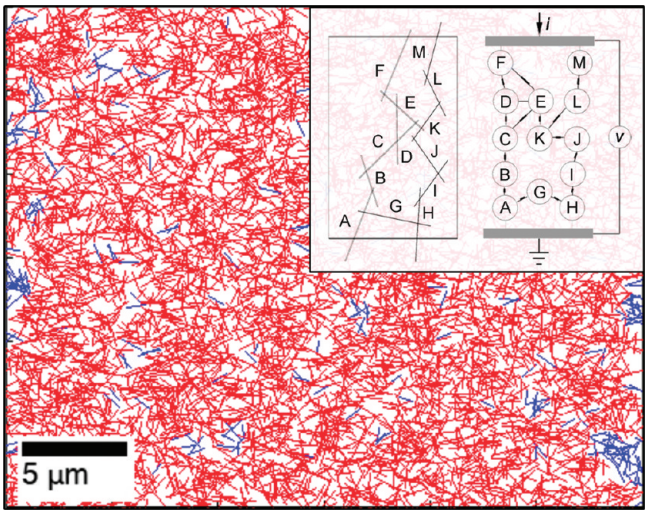

Figure 5. Simulated bundle network consisting of randomly oriented line segments with a log-normal length distribution. The red and blue colors denote segments that form conducting pathways and segments that do not, respectively. The inset displays how the resistor network is formed out of line segments and their intersections, with the simulated input current *i* and induced voltage *v* indicated.

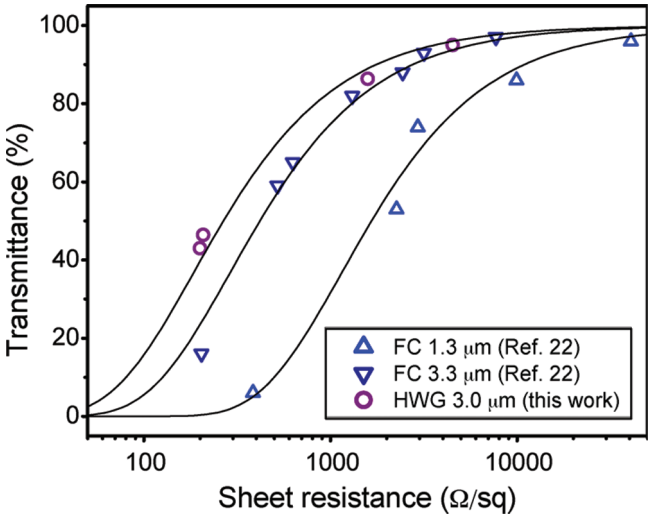

Figure 6. Sheet resistance versus transmittance at 550 nm for undoped sample sets from the ferrocene reactor with two different bundle length distributions (FC, ref 22) and the hot wire generator reactor (HWG, this work). Solid lines show fits based on eq 3, with figure of merit *K* as the fitting parameter.

(so-called ferrocene reactor,[22] denoted here by FC), with bundle length distributions of 1.3 ± 0.8 μm (upward blue triangles in Figure 6) as well as 3.3 ± 1.4 μm (downward dark blue triangles), and bundle diameter distributions of 8.3 ± 3.5 nm and 7.8 ± 2.7 nm, respectively. Additionally, four undoped films synthesized with the HWG reactor using the same conditions as the 0 ppm NH_3 sample constituted another undoped sample set (purple circles). Optical transmittance and sheet resistance data measured from these undoped films together with fits based on eq 3 are shown as Figure 6 (see also Table S1 of the Supporting Information).

The figures of merit of the undoped sample sets were calculated from fits of eq 3 to the data in Figure 6 and are plotted

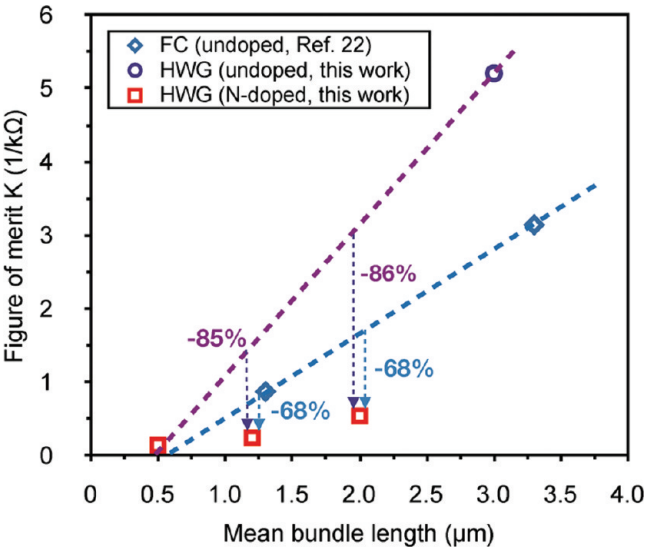

Figure 7. Figures of merit versus mean bundle lengths for undoped sample sets from the ferrocene (blue diamonds, ref 22) and HWG (purple circles, this work) reactors and nitrogen-doped films from the HWG reactor (red squares, Table 1). The purple thick dotted line is a linear fit to the undoped and 300 ppm NH_3 doped HWG sample, while the blue thick dotted line is a linear fit to the undoped ferrocene samples. The vertical dotted lines represent the deficits of the figures of merit of the doped films compared to the ferrocene data (blue) and the undoped HWG data (purple).

in Figure 7, along with the values calculated for each of the doped samples (Table 1). Thus, the undoped sample data points (blue diamonds and purple circles) are derived from several films (Figure 6), while the doped sample data points correspond simply to the samples in Table 1. From Figure 7, we can see that the figures of merit of the doped samples are lower compared to those of undoped sample sets with similar length distributions collected from either the ferrocene reactor (blue dotted line) with a deficit of 68% for the 100 and 200 ppm samples. Furthermore, if we compare the values of the doped films to the undoped HWG data (dotted purple line), the deficit is 85−86%. For both kinds of films, the intercept of the *x*-axis is around 0.5 μm, which might indicate the onset of the percolation threshold, in agreement with the simulations (Figure S4 of the Supporting Information).

Remarkably, the undoped HWG films show even better optoelectronic properties than the previously reported ferrocene reactor films.[22] The higher performance of the undoped HWG samples compared to that of the ferrocene samples (with ~3 μm bundle length) can likely be explained by the smaller bundle diameter of the HWG samples and thus smaller contact resistances between the bundles. Because the figure of merit *K* scales inversely with the contact resistance, we see that the undoped HWG data point would agree with the ferrocene data if we assumed that the contact resistances were 50% lower for the smaller HWG bundles. Nirmalraj et al. estimated[38] the resistance drop to be roughly 70% for the bundle diameters measured here (7.8 and 6.1 nm for the ferrocene and HWG samples, respectively); though we note that our largest bundles are at the lower end of their largest diameter category. Most importantly in the context of this work, we note that should the bundles of doped nanotubes with even smaller bundle diameters exhibit smaller contact resistances than the undoped ones, this would only serve to further increase the deficit observed here.

5. DISCUSSION

Considering the optical absorption (Figure 2) and Raman (Figure 3) spectra of the 100 ppm NH_3 sample, they seem to be intermediate between the 0 and 200 ppm NH_3 spectra. By contrast, there is little change from the 200 to the 300 ppm NH_3 spectra, even though the bundles are getting shorter still (Table 1). Thus, it seems that full modification of nanotube properties can be achieved already with 200 ppm, while 300 ppm affects the growth excessively. This is also seen in the EELS measurements, where the 300 ppm sample was unstable under the electron beam in EELS.

If the nitrogen feedrate was too large (above 300 ppm, in this case), nanotube growth was terminated. This could be either due to a saturation and breakdown of the hexagonal carbon network by nitrogen or to nitrogen blocking the adsorption sites on the cluster and preventing the sufficient input of further carbon,[48] slowing down and eventually stopping the growth. Another scenario is that NH_3 accelerates the production of active gaseous compounds, which compete with sp^2 bond formation (etching effect). Either possibility could explain the sudden termination of production with over 300 ppm NH_3. The observed shortening of bundles with increasing ammonia concentration could be attributable either to a decrease in the growth rate or to an earlier termination of growth as discussed above. The growth mechanism of N-SWCNTs will be addressed in a future publication.

Our theoretical resistor network model suggests that in a dense network (far from the percolation threshold, i.e., the minimum density where conducting paths are formed) of CNT bundles or similar conductors, where the resistance of bundle-to-bundle contacts dominates, the network conductance scales linearly with the average bundle length. This result is in line with earlier electronic measurements of CNT networks far above the percolation threshold[49] and data obtained from the undoped ferrocene samples.[22]

As for the electrical properties of the films, the analysis of Section 4.2 indicates that shortening bundle lengths alone were not enough to explain the drastically increasing sheet resistances with increasing levels of ammonia. On the basis of our network simulations and the undoped samples with different bundle lengths, we could estimate that the figures of merit K (eq 3) of the 100 and 200 ppm NH_3 films were between 68% and 86% times smaller than would be expected on the basis of their measured average bundle lengths. Thus, the measured resistances of the 100 and 200 ppm NH_3 films were 5 to 10 times larger than expected. The 300 ppm NH_3 bundles were already so short that they likely do not form a proper percolating network, and the analysis is no longer applicable.

If we assume that the N dopants do not increase the junction resistances (rather, it has been suggested they could even decrease them[50]), it seems clear that the conductivities of the bundles themselves decrease with doping. This can perhaps be attributed to an increasing number of randomly distributed scattering centers in the doped nanotubes, which decrease the mean free paths of the carriers.[7,8,51,52] Latil and co-workers have theoretically shown that the mean free path decreases linearly with dopant concentration at low (<0.5%) doping levels.[53] Whether the experimental effect observed here is due to an increased number of defects not related to nitrogen or the actual dopant sites themselves is a topic for further research, though the nonincreasing intensity of the Raman D band (Figure 3) would not suggest that the defect density is significantly increased. However, we note that the bundles of doped tubes seem to show fewer impurities on their surfaces, which could affect the measurements.

Because the resistance measurements were conducted in air in ambient conditions, it is conceivable that the p-type doping from the environment could affect the results. However, all the resistance values were measured within hours of collecting the samples, and because environmental doping is very slow, it can be disregarded here.

Note that the effect of local dopants can be different in N-SWCNTs than in the more studied N-MWCNT case, where it has been demonstrated that the dopants increase the number of charge carriers and enhance the conductance.[27,54] Only very few studies have tried to experimentally address the issue of the conductivity of N-SWCNTs.[17,41,55] The results thus far are neither conclusive nor comprehensive, and clearly more work is needed. Single tube transport or network transistor measurements would likely help elucidate the microscopic mechanism for the effect observed here for macroscopic films.

6. CONCLUSIONS

Nitrogen-doped single-walled carbon nanotubes were synthesized using an aerosol floating catalyst CVD method and deposited on different substrates as grown directly as films. A variety of spectroscopic methods indicates the presence of nitrogen in the nanotubes. Analysis of the optoelectronic properties of the films shows that their sheet resistances are significantly higher than would be expected from their geometrical connectivity. This suggests that the intratube resistances are higher for doped tubes than for undoped tubes. Our work represents the first experimental report on macroscopic films of N-SWCNT of which we are aware.

■ ASSOCIATED CONTENT

Ⓢ Supporting Information. TEM micrographs of SWCNTs synthesized with 0 and 200 ppm NH_3, along with line profiles for determining the diameters; nanotube diameter distributions of the 200 ppm NH_3 sample determined by OAS and TEM; and the simulated network conductance as a function of average line segment length. This material is available free of charge via the Internet at http://pubs.acs.org.

■ AUTHOR INFORMATION

Corresponding Author

*E-mail: toma.susi@tkk.fi (T.S.), esko.kauppinen@tkk.fi (E.I.K.). Phone: +358 50 344 1574 (T.S.), +358 40 509 8064 (E.I.K.). Fax: +358 9 451 3517.

■ ACKNOWLEDGMENT

We gratefully acknowledge the valuable feedback from M. Kalbác and thank S. Riikonen, L. Peltonen, S. Seppälä, and M.J. Alava for fruitful discussions. We are also indebted to the reviewers of the manuscript for their invaluable input for improving the quality of this work.

This work has been supported in part by the European Commission under the FP6 (STREP project BNC Tubes, contract NMP4-CT-2006-03350), Academy of Finland (project 128445), Finnish TEKES GROCO Project (1298/31/08), and the Aalto University MIDE-program project CNB-E. R.

A. and A.L. have also been supported by the ANR PNANO program (Project Cedona, contract ANR-07-NANO-007-02), T. P. by the Austrian Science Fund FWF P21333-N20, and P.A. by a Marie Curie Intra-European Fellowship within the seventh European Community Framework Programme.

REFERENCES

(1) Li, X.; Tu, X.; Zaric, S.; Welsher, K.; Seo, W. S.; Zhao, W.; Dai, H. *J. Am. Chem. Soc.* **2007**, *129*, 15770.
(2) Ding, L.; Tselev, A.; Wang, J.; Yuan, D.; Chu, H.; McNicholas, T. P.; Li, Y.; Liu, J. *Nano Lett.* **2009**, *9*, 800.
(3) Bachilo, S. M.; Balzano, L.; Herrera, J. E.; Pompeo, F.; Resasco, D. E.; Weisman, R. B. *J. Am. Chem. Soc.* **2003**, *125*, 11186.
(4) Jasti, R.; Bertozzi, C. R. *Chem. Phys. Lett.* **2010**, *494*, 1.
(5) Yi, J. Y.; Bernholc, J. *Phys. Rev. B* **1993**, *47*, 1708.
(6) Stephan, O.; Ajayan, P. M.; Colliex, C.; Redlich, P.; Lambert, J. M.; Bernier, P.; Lefin, P. *Science* **1994**, *266*, 1683.
(7) Ma, J.; Guan, S.; Lai, C.-H. *Phys. Rev. B* **2006**, *74*, 205401.
(8) Choi, H. J.; Ihm, J.; Louie, S. G.; Cohen, M. L. *Phys. Rev. Lett.* **2000**, *84*, 2917.
(9) Ayala, P.; Arenal, R.; Loiseau, A.; Rubio, A.; Pichler, T. *Rev. Mod. Phys.* **2010**, *82*, 43.
(10) Arenal, R.; Blase, X.; Loiseau, A. *Adv. Phys.* **2010**, *59*, 101.
(11) Yu, D.; Nagelli, E.; Du, F.; Dai, L. J. *Phys. Chem. Lett.* **2010**, *1*, 2165.
(12) Ayala, P.; Arenal, R.; Rümmeli, M. H.; Rubio, A.; Pichler, T. *Carbon* **2010**, *48*, 585.
(13) Ewels, C. P.; Glerup, M. J. *Nanosci. Nanotechnol.* **2005**, *5*, 1345.
(14) Glerup, M.; Steinmetz, J.; Samaille, D.; Stephan, O.; Enouz, S.; Loiseau, A.; Roth, S.; Bernier, P. *Chem. Phys. Lett.* **2004**, *387*, 193.
(15) Ayala, P.; Gruneis, A.; Gemming, T.; Grimm, D.; Kramberger, C.; Rummeli, M. H.; Freire, F. L., Jr; Kuzmany, H.; Pfeiffer, R.; Barreiro, A. J. *Phys. Chem. C* **2007**, *111*, 2879.
(16) Lin, H.; Arenal, R.; Enouz-Vedrenne, S.; Stephan, O.; Loiseau, A. J. *Phys. Chem. C* **2009**, *113*, 9509.
(17) Villalpando-Paez, F.; Zamudio, A.; Elias, A. L.; Son, H.; Barros, E. B.; Chou, S. G.; Kim, Y. A.; Muramatsu, H.; Hayashi, T.; Kong, J.; Terrones, H.; Dresselhaus, G.; Endo, M.; Terrones, M.; Dresselhaus, M. S. *Chem. Phys. Lett.* **2006**, *424*, 345.
(18) Ayala, P.; Grüneis, A.; Kramberger, C.; Rümmeli, M. H.; Solorzano, I. G.; Freire, F. L., Jr; Pichler, T. J. *Chem. Phys.* **2007**, *127*, 184709.
(19) Min, Y. S.; Bae, E. J.; Asanov, I. P.; Kim, U. J.; Park, W. *Nanotechnology* **2007**, *18*, 285601.
(20) Keskar, G.; Rao, R.; Luo, J.; Hudson, J.; Chen, J.; Rao, A. M. *Chem. Phys. Lett.* **2005**, *412*, 269.
(21) Wu, Z.; Chen, Z.; Du, X.; Logan, J. M.; Sippel, J.; Nikolou, M.; Kamaras, K.; Reynolds, J. R.; Tanner, D. B.; Hebard, A. F.; Rinzler, A. G. *Science* **2004**, *305*, 1273.
(22) Kaskela, A.; Nasibulin, A.; Timmermans, M.; Aitchison, B.; Papadimitratos, A.; Tian, Y.; Jiang, H.; Brown, D.; Zakhidov, A.; Kauppinen, E. *Nano Lett.* **2010**, *10*, 4349.
(23) Artukovic, E.; Kaempgen, M.; Hecht, D. S.; Roth, S.; Grüner, G. *Nano Lett.* **2005**, *5*, 757.
(24) Zavodchikova, M. Y.; Kulmala, T.; Nasibulin, A. G.; Ermolov, V.; Franssila, S.; Grigoras, K.; Kauppinen, E. I. *Nanotechnology* **2009**, *20*, 085201.
(25) Aguirre, C. M.; Auvray, S.; Pigeon, S.; Izquierdo, R.; Desjardins, P.; Martel, R. *Appl. Phys. Lett.* **2006**, *88*, 183104.
(26) Snow, E. S.; Perkins, F. K.; Houser, E. J.; Badescu, S. C.; Reinecke, T. L. *Science* **2005**, *307*, 1942.
(27) Wiggins-Camacho, J.; Stevenson, K. J. *Phys. Chem. C* **2009**, *113*, 9.
(28) Nasibulin, A. G.; Moisala, A.; Brown, D.; Jiang, H.; Kauppinen, E. I. *Chem. Phys. Lett.* **2005**, *402*, 227.
(29) Susi, T.; Nasibulin, A. G.; Ayala, P.; Tian, Y.; Zhu, Z.; Jiang, H.; Roquelet, C.; Garrot, D.; Lauret, J. S.; Kauppinen, E. I. *Phys. Status Solidi B* **2009**, *246*, 2507.
(30) Panchalkarla, L. S.; Govindaraj, A.; Rao, C. N. R. *ACS Nano* **2007**, *1*, 494.
(31) Susi, T.; Zhu, Z.; Ruiz-Soria, G.; Arenal, R.; Ayala, P.; Nasibulin, A. G.; Lin, H.; Jiang, H.; Stephan, O.; Pichler, T.; Loiseau, A.; Kauppinen, E. I. *Phys. Status Solidi B* **2010**, *247*, 2726.
(32) Huang, J.; Zhang, Q.; Zhao, M.; Wei, F. *Nano Res.* **2009**, *2*, 872.
(33) Nasibulin, A. G.; Brown, D. P.; Queipo, P.; Gonzalez, D.; Jiang, H.; Kauppinen, E. I. *Chem. Phys. Lett.* **2006**, *417*, 179.
(34) Arenal, R.; De la Pena, F.; Stephan, O.; Walls, M.; Tence, M.; Loiseau, A.; Colliex, C. *Ultramicroscopy* **2008**, *109*, 32.
(35) Jeanguillaume, C.; Colliex, C. *Ultramicroscopy* **1989**, *28*, 252.
(36) Lyons, P. E.; De, S.; Blighe, F.; Nicolosi, V.; Pereira, L. F. C.; Ferreira, M. S.; Coleman, J. N. *J. Appl. Phys.* **2008**, *104*, 044302.
(37) de Pablo, P. J.; Martínez, M. T.; Colchero, J.; Gómez-Herrero, J.; Maser, W. K.; Benito, A. M.; Muñoz, E.; Baró, A. M. *Adv. Mater.* **2000**, *12*, 573.
(38) Nirmalraj, P. N.; Lyons, P. E.; De, S.; Coleman, J. N.; Boland, J. J. *Nano Lett.* **2009**, *9*, 6.
(39) Liu, X.; Pichler, T.; Knupfer, M.; Golden, M. S.; Fink, J.; Kataura, H.; Achiba, Y. *Phys. Rev. B* **2002**, *66*, 045411.
(40) Tian, Y.; Jiang, H.; Pfaler, J. v.; Zhu, Z.; Nasibulin, A. G.; Nikitin, T.; Aitchison, B.; Khriachtchev, L.; Brown, D. P.; Kauppinen, E. I. J. *Phys. Chem. Lett.* **2010**, *1*, 1143.
(41) Ibrahim, E.; Khavrus, V.; Leonhardt, A. *Diamond Relat. Mater.* **2010**, *19*, 1199.
(42) Jorio, A.; Saito, R.; Dresselhaus, G.; Dresselhaus, M. S. *Philos. Trans. R. Soc., A* **2004**, *362*, 2311.
(43) Maciel, I. O.; Anderson, N.; Pimenta, M. A.; Hartschuh, A.; Qian, H.; Terrones, M.; Terrones, H.; Campos-Delgado, J.; Rao, A. M.; Novotny, L.; Jorio, A. *Nat. Mater.* **2008**, *7*, 878.
(44) Souza Filho, A. G.; Jorio, A.; Samsonidze, G. G.; Dresselhaus, G.; Pimenta, M. A.; Dresselhaus, M. S.; Swan, A. K.; Uuml, nl; S., M.; Goldberg, B. B.; Saito, R. *Phys. Rev. B* **2003**, *67*, 035427.
(45) Kalbac, M.; Kavan, L. *Carbon* **2010**, *48*, 7.
(46) Ayala, P.; Miyata, Y.; De Blauwe, K.; Shiozawa, H.; Feng, Y.; Yanagi, K.; Kramberger, C.; Silva, S.; Follath, R.; Kataura, H. *Phys. Rev. B* **2009**, *80*, 205427.
(47) Elias, A. L.; Ayala, P.; Zamudio, A.; Grobosch, M.; Cruz-Silva, E.; Romo-Herrera, J. M.; Campos-Delgado, J.; Terrones, H.; Pichler, T.; Terrones, M. J. *Nanosci. Nanotechnol.* **2010**, *10*, 3959.
(48) Harutyunyan, A.; Awasthi, N.; Jiang, A.; Setyawan, W.; Mora, E.; Tokune, T.; Bolton, K.; Curtarolo, S. *Phys. Rev. Lett.* **2008**, *100*, 195502.
(49) Snow, E. S.; Novak, J. P.; Campbell, P. M.; Park, D. *Appl. Phys. Lett.* **2003**, *82*, 2145.
(50) Nevidomskyy, A. H.; Csányi, G.; Payne, M. C. *Phys. Rev. Lett.* **2003**, *91*, 105502.
(51) Avriller, R.; Latil, S.; Triozon, F.; Blase, X.; Roche, S. *Phys. Rev. B* **2006**, *74*, 121406.
(52) Lopez-Bezanilla, A.; Blase, X.; Roche, S. *Nano Res.* **2010**, *3*, 288.
(53) Latil, S.; Roche, S.; Mayou, D.; Charlier, J.-C. *Phys. Rev. Lett.* **2004**, *92*, 256805.
(54) Czerw, R.; Terrones, M.; Charlier, J. C.; Blase, X.; Foley, B.; Kamalakaran, R.; Grobert, N.; Terrones, H.; Tekleab, D.; Ajayan, P. M.; Blau, W.; Ruhle, M.; Carroll, D. L. *Nano Lett.* **2001**, *1*, 457.
(55) Krstic, V.; Rikken, G. L. J. A.; Bernier, P.; Roth, S.; Glerup, M. *Europhys. Lett.* **2007**, 77.